PCCP

Accepted Manuscript

ROYAL SOCIETY OF CHEMISTRY

www.rsc.org/pccp

Computational Modeling of Self-Trapped Electrons in Rutile TiO_2

Likai Yan[†‡], Justin E. Elenewski,[‡] Jiang Wei[§] and Hanning Chen*[‡]

[†]: Department of Chemistry, Northeast Normal University, Changchun 130024, the People's Republic of China

[‡]: Department of Chemistry, the George Washington University, Washington, DC 20052, the Untied States of America

[§]: Argonne Leadership Computing Facility, Argonne National Laboratory, Argonne, IL 60439, the Untied States of America

*: corresponding author

800 22nd Street, NW, Washington, DC 20052

Fax: 202-994-5873

Phone: 202-992-4492

Email: chenhanning@gwu.edu

Abstract

In conjunction with the constrained density functional theory, a valence-bond representation has been employed to model the migration of anionic polaron in bulk rutile TiO_2. It was found that the charge delocalization of a self-trapped electron proceeded predominately along the *c* crystal axis of rutile, thus exhibiting pronounced directional heterogeneity of polaron migration. As a result, the extrapolated polaron activation energies are 0.026 eV and 0.195 eV along the [001] and [111] lattice vectors, respectively. According to the Holstein theory, the difference on the activation energy makes the polaron drift over 100 times faster along the *c* crystal axis than on the *ab* crystal plane at room temperature. The notable anisotropy of the anionic polaron was also reflected through the electron paramagnetic resonance (EPR) *g*-matrix, whose principal component along [001] is substantially smaller than that along [110] or [$1\,\bar{1}\,0$]. Finally, the extent of polaron charge was probed by our calculated isotropic hyperfine coupling constants on two groups of crystallographically inequivalent ^{17}O atoms, which manifest distinct strengths of spin-orbit interaction with the unpaired electron.

Keywords: polaron migration, valence bond theory, electron transfer, charge mobility

1. Introduction:

Titania, TiO_2, has been widely considered as a model system to study photoinduced charge migration in wide-band semiconductors since the world's first photocatalytic water-splitting experiment[1] was reported in 1972 by using an n-type TiO_2 electrode as both light harvester and electrical conductor. Among the three naturally occurring TiO_2 polymorphs, rutile is more thermodynamically stable than metastable phases of anatase and brookite at all temperatures.[2-3] Consequently, the phase transformation from anatase (or brookite) to rutile can proceed spontaneously under rather mild reaction conditions of 400 K and 1 atmosphere.[4] Because of its relatively small molar volume of 18.79 cm^3/mol,[5] rutile is also the primary titanium-bearing polymorph in many high-pressure metamorphic rocks, including eclogites[6] and amphibolites.[7] For example, rutile is the second most abundant heavy mineral sand after limenite.[8] In the form of fine powder, rutile is brilliant white due to its high refractive index of ~2.70,[9] making it an ideal coating material[10] for many optoelectronic devices, such as optical fibers, laser diodes and charge-coupled image sensors. Since the optical scattering coefficient of rutile[11] is notably greater than those in anatase[12] and brookite[13] over a wide range of incident wavelengths, rutile has also been used as opaque pigments[14] in painting supplies. Moreover, in a recent biomedical study,[15] rutile nanoparticles exhibit excellent effectiveness of protecting human skin from ultraviolet and visible light irradiation. With regard to its non-toxicity and aesthetical appeal, rutile is potentially useful for sunscreen formulation.[16] Nevertheless, the fastest growing application of rutile is on photovoltaic cells wherein the electron collection layers are

preferably made of nanocrystalline rutile thin films in light of their extraordinarily high electron mobility on the order of $cm^2/V•sec$ at room temperature.[17-18]

In a complete cycle of photovoltaic conversion, an electron-hole pair is first generated upon light absorption before the dissociated electron and hole migrate to two opposite electrodes to sustain an electric current in an external circuit. A key process to dictate the overall conversion efficiency is the charge migration in semiconducting films whose desired traits include not only high mobility but also easy controllability of migration direction. For instance, the rutile [001] surface exhibits a much better efficiency than both the rutile [110] and [100] surfaces on photocatalytic methanol oxidation to formaldehyde.[19] However, since rutile [001] surface is also the least thermodynamically stable, a rutile nanoparticle usually possesses a large percentage of [110] and [100] surfaces,[20] making the typical photocatalytic activity of rutile significantly lower than anatase. In another surface-specific study by intensity modulated photocurrent spectroscopy, the rutile [001] surface was also found to be an excellent photocatalyst, surpassing other surfaces for water oxidation[21]when being aided by hydroxide anions. Although the photocatalytic efficiency of different rutile surfaces is primarily determined by their reconstructed atomistic structures,[22] the directional heterogeneity in charge mobility is also believed to be essential.[23] In a photoconductivity study,[18] the excited electrons were observed to drift preferentially along the *c* axis of a rutile crystal at all temperatures. This anisotropy was later confirmed by examining the dependence of the relative thermoelectric power of rutile on its electrical resistance.[17] In spite of many pioneering experimental and theoretical investigations,[24-25] a comprehensive explanation of this interesting anisotropy of electron mobility remains

elusive, and it continues to draw attention from materials research community. For example, both hybrid density functional theory (DFT) and direct random phase approximation (RPA) have been applied recently to model electron trapping in bulk rutile by empirically varying the fraction of Hartree-Fock (HF) exchange in the energy functional.[26]

At present, the most widely used methodology to investigate polaron migration is the Emin-Holstein-Austin-Mott (EHAM) theory,[27-28] which relates charge hopping rate in a deformable continuum to the associated diabatic reorganization energy and electronic coupling strength. For instance, in a DFT+*U* study[24] on electron transport in bulk anatase and rutile, an effective *U* parameter of 10.0 eV has to be applied to fully localize the transferring electron on Ti *3d* orbitals. Although the DFT+*U* method is computationally efficient, it is rather difficult to have a universal *U* parameter that will yield satisfactory results for all physical properties of a given system. The difficulty primarily arises from the distinct overlocalization tendencies of molecular orbitals due to the self-interaction errors[29] in DFT. A plausible alternative to DFT+*U* is RPA, which can be regarded as a non-perturbative form of coupled cluster theory.[30] In RPA, the electron correlation energy is explicitly inferred from the adiabatic transition densities between the occupied and unoccupied reference orbitals,[31] making it well suited for polaronic systems where the energy gap between excess electrons (or holes) and conduction (or valence) band is usually small. As an example, the RPA-calculated polaron formation energies of bulk anatase and rutile are nearly independent to the underlying DFT functionals,[26] suggesting that the electron correlation between Ti *3d* orbitals is sufficiently captured.[32] Another wavefunction-based treatment of polaron is the complete active electronic self-consistent-

field (CASSCF) method[33] wherein the polaron wavefunction is represented as a linear combination of high-spin and low-spin states, yielding accurately determined electronic coupling strength. For example, in the (001) plane of chromia, α-Cr_2O_3, the electronic coupling strength between the two high-spin states of the $Cr^{II} + Cr^{III} \rightarrow Cr^{III} + Cr^{II}$ reaction is substantially greater than that between the two low-spin states,[34] confirming the smaller size of low-spin Cr^{II} cations compared to the high-spin ones.[35] By contrast, for the reaction of $Cr^{III} + Cr^{IV} \rightarrow Cr^{IV} + Cr^{III}$, these two spin configurations only differ by ~5% on the electronic coupling strength. Although the RPA and CASSCF methods can be employed to treat periodic systems using the hybrid Gaussian and plane wave (GPW) scheme[36] and Wannier transformation,[37] respectively, their computational cost is very demanding for defective supercells, which must be large enough to alleviate the boundary artifacts due to crystalline distortion. Aiming to achieve a comprised balance between computational efficiency and theoretical soundness, a valence-bond (VB) representation of polaron has been developed[38] on the basis of constrained density functional theory (CDFT).[39] As shown by its application to bulk anatase,[38] the VB representation not only explains the pronounced directional heterogeneity in charge migration, but also obtains polaron mobilities that are in excellent agreement with experiments at different temperatures. In the present study, the VB representation will be extended to investigate the migration of self-trapped electrons in bulk rutile, the most-produced TiO_2 polymorph.

2. Simulation Methods:

In our VB representation,[38] a polaron, $\Psi = \sum c_i \varphi_i$, is formulated as a linear combination of some single-site charged complexes (abbreviated as complexes

thereafter), $\{\varphi\}$, each of which consists of a pivotal atom and all of its adjacent atoms that are chemically bonded together. For bulk rutile whose conduction band is mostly comprised of Ti *3d* orbitals (Fig. 1), an electron (or anionic) complex includes a pivotal titanium atom and six coordinated oxygen atoms (Fig. 2). Therefore, a complex's charge, Q_c, can be defined as $Q_c = Q_p + \frac{1}{N_C}\sum_{i=1}^{N_C} Q_i$, where N_C is the coordination number of 6, Q_P is the charge of the pivotal titanium atom, and Q_i is the charge of its *i* th coordinated oxygen atom. In the present study, the CDFT[39] was applied to impose the density derived atomic point charge (DDAPC)[40] constraints to the titanium-centered complexes. Due to the electron-phonon coupling, the imposed charge constrains invalidates the Born-Oppenheimer approximation,[41] resulting in polaron delocalization. According to the VB theory, the extent of polaron delocalization is effectively reflected by the combination coefficients, $C = \{c_i\}$, which can be uniquely determined by matrix diagonalization: $HC = \varepsilon SC$, where H and S are the Hamiltonian and overlap matrices, respectively, and ε is the delocalization energy. The diagonal terms of matrix H correspond to the electron transfer reorganization energy, defined in reference to a super cell that is geometrically optimized with respect to a polaron with inclusive charge of $Q_C = -1$ on a designated complex. This is termed the pivotal reduced complex assigned an index of 1. Thus, $H_{ii} = E(Q_i, R_1) - E(Q_1, R_1)$, where Q_i indicates the location of the inclusive polaron charge and R_1 is the optimized geometry of the pivotal reduced complex. Using a given off-diagonal term of matrix H, the electronic coupling strength between two corresponding complexes can be evaluated by a method based on orthogonal orbital transformation:[42]

$$H_{ij} = \frac{V_{ij} - S_{ij}\left(H_{ii} + H_{jj}\right)/2}{1 - S_{ij}^2} \quad (1)$$

where $V_{ij} = \left\langle \varphi_i \middle| \hat{H}_0 \middle| \varphi_j \right\rangle$ and $S_{ij} = \left\langle \varphi_i \middle| \varphi_j \right\rangle$. Because both V_{ij} and S_{ij} refer to the parameters on the dividing plane between two diabatic states, they are evaluated for a transition state geometry that is optimized under a mixed Hamiltonian:

$$\hat{H}_{ij} = \frac{1}{2}\hat{H}_i + \frac{1}{2}\hat{H}_j \quad (2)$$

where i and j mark the locations of the inclusive polaron charge. Although a complete basis set of our VB representation requires the inclusion of all complexes in a super cell, only those with a considerable share of the polaron charge will be considered in practice. Furthermore, if a pair of complexes is not bridged by any common atom, their electronic coupling strength and orbital overlap are assumed to be zero with regard to their rapid decay over distance.

Unless otherwise specified, all simulations in the present study are performed using CP2K software[36] with the Geodecker-Teter-Huter (GTH) pseudopotential,[43] Perdew-Burke-Ernzehof (PBE) exchange-correlation functional[44] and polarized-valence-double-ζ (PVDZ) basis set.[45] Moreover, the DFT+U method is adopted to account for the electron correlation effects by adding an on-site Hubbard potential, U, to the titanium *3d* orbitals. The optimal value of U is determined using the hybrid functional of PBE0 [46] as a reference for the overlap matrix element, S_{ij}, between two adjacent complexes along the [001] lattice vector, which is chosen for the shortest Ti-Ti distance. As shown in Fig. 3, S_{ij} drops rapidly from 0.88 to 0.57 as U increases from 1.0 eV to 4.5 eV when using a small $3\times3\times7$ benchmark supercell. The optimal U is found to be approximately 2.5 eV

and that is assumed for all production simulations in the larger $3\times3\times11$ super cell. The overlap matrix element is chosen as our gauging property because conventional DFT usually yields overly delocalized electrons due to self-interaction errors.[29] In fact, a Hubbard potential of $U = 2.5$ eV was used in a previous DFT+U study[47] of defected bulk rutile, achieving excellent agreement with experimental dopant energy levels. Note that the benchmark and production super cells both have a total net charge of -1, requiring spin-unrestricted DFT calculations for those open-shell systems.

3. Simulation Results:

The pivotal reduced complex shares common oxygen atom(s) with each of the two adjacent complexes along the [001] direction, as well as with each of the eight adjacent complexes along the [111] direction (Fig. 4), making H and S 11×11 matrices (See Supporting Information S1 and S2) after disregarding all non-bridged complexes. Since each of the companion [001] complexes is connected to the pivotal one through a pair of bridge oxygen atoms, the associated electronic coupling strength turns out to be -71.06 eV, which is more than two orders of magnitude greater than that between the pivotal and [111] complexes. The remarkable directional heterogeneity on polaron delocalization is also reflected through the overlap matrix elements with a nontrivial value of $S_{ij} = 0.761$ along [001] and a nearly negligible $S_{ij} = 0.015$ along [111]. After diagonalizaing the overlap-weighted Hamiltonian matrix, $S^{-1}H$, the polaron charge distribution is then given by the diagonal terms of $C^{\dagger}CS$. As illustrated in Fig. 4, the pivotal reduced complex and its two adjacent [001] neighbors bear ~99.98% of the excess electron, justifying the exclusion of all [111] complexes in the polaron basis set for

subsequent discussions. Moreover, a substantial 24.2% of the polaron charge is held by each of the two adjacent [001] complexes, suggesting that a further charge delocalization may occur to the second nearest complexes and beyond along the c crystal axis.

Aiming to examine the completeness of the polaron charge delocalization, the polaron basis set is incrementally expanded through the pairwise addition of chemically equivalent [001] complexes. As a result, a total of five systems labeled as RTn $\{n=1...5\}$ are constructed by including up to the *n*-th nearest [001] neighbors of the pivotal reduced complex (Fig. 5). While sequentially added complexes continue to carry additional polaron charge, the quantity carried by an outermost complex drops drastically from -0.242 in RT1 to -0.009 in RT5, demonstrating a rapid stabilization of electron-phonon coupling. By far, the greatest change is always observed on the pivotal reduced complex, whose net charge decreases from -0.516 in RT1 to -0.202 in RT5, confirming the instability of Ti^{3+} cations in reduced rutile.[48] A natural measure of an electron's extent of delocalization is its effective radius, which is defined as:

$$r_e^2 = \int \left(r - R_n(r)\right)^2 \varphi_e^*(r)\varphi(r)dr \qquad (3)$$

where $\varphi_e(r)$ is the electron wavefunction at a given position, r, and $R_n(r)$ is the coordinate of the nearest nucleus. Similarly, the effective radius of an anionic polaron, r_P, can be estimated using the system's highest occupied molecular orbital (HOMO) as the polaron's wavefunction. When the polaron charge is forced to reside within the pivotal reduced complex, the calculated r_P is 0.66Å with this effective radius increasing to 0.77Å in RT5 after sufficient charge delocalization. Both determinations are in excellent agreement with 0.67Å, the theoretical radius of an isolated Ti^{3+} cation,[49] and 0.76Å, the experimental value for a six-coordinated Ti^{3+} cation in crystal.[50] Therefore, the expansion

of polaron can be ascribed to the increasing covalent-like characteristics of the Ti-O bonds in all participant complexes.

According to the Holstein polaron theory,[51-52] extensive charge delocalization results in shallow polarons, which are characterized by a diminished activation energy for lattice hopping. As an example, an electron trapped by laser-induced defects in bulk rutile is only thermally stable below 15 K. At higher temperatures, the electron paramagnetic resonance (EPR) signal for the trapped electrons decreases significantly in intensity due to the recombination of thermally mobilized electrons and holes.[48, 53] Obviously, the activation energy, ΔG^*, of a polaron depends on its migration direction, and can be evaluated by

$$\Delta G^* = E(R_{TS}) - E(R_P) \qquad (4)$$

where $E(R_P)$ is the energy of an optimized polaron, and R_{TS} is the optimized transition state with Hamiltonian given by Eq.2. For each of the five RT*n* systems, the calculated polaron activation energies along the [001] and [111] lattice vectors are shown in Fig. 6a and Fig. 6b, respectively. It is not surprising that ΔG^*s decay rapidly upon charge delocalization in both directions. For example, ΔG^* decreases from 0.352 eV in RT1 to 0.031 eV in RT5 along c crystal axis. Exponential fitting this dependence for ΔG^* yields an asymptotic value of 0.026 eV, which is only 0.002 eV greater than the experimental activation energy if the polaron migration is assumed to proceed predominantly along [001]. By contrast, a much greater exponential asymptote of 0.195 eV is observed for ΔG^* along [111], underscoring our assumptions. The pronounced anisotropy in polaron migration is also revealed by the charge motility calculation using the Einstein relation:[54]

$$\mu = \frac{eR^2 n k_p}{k_B T} = \frac{eR^2 n}{k_B T} \omega_0 e^{-\Delta G^*/k_B T} \quad (5)$$

where e is the elementary charge, n is the number of equivalent polaron accepting sites, R is the distance between the reaction and product polarons, k_p is the polaron hopping rate, and ω_0 is the phonon angular frequency. Under the single-phonon approximation, a vibrational energy of $\hbar\omega_0 = 0.10$ eV is selected to reflect the longitudinal optical phonon modes in bulk rutile.[32, 55] As listed in Table 1, the polaron drift is over 100 times faster along [001] than that along [111] at room temperature. After projecting the calculated mobilities onto the three crystal lattices, we find that $\mu_a = \mu_b = 0.02$ cm^2/V•s and $\mu_c = 3.78$ cm^2/V•s. The latter value is well in line with the experimental estimate by Terahertz spectroscopy.[56] Compared to anatase,[38] rutile exhibits not only a higher electron mobility but also a more notable directional heterogeneity as quantified by the ratio between μ_c and μ_a (or μ_b). It is also interesting to note that our calculated mobilities, μ, are not sensitive to the choice of U. When U is varied by 1.0 eV, ΔG^* only undergoes a small change of ~0.003 eV (Supporting Information S3), which is approximately a tenth of $k_B T$ at room temperature. The insensitivity originates from the shift of the reactant and transition states' energies to a similar extent by the on-site Hubbard potential.

EPR has become a powerful tool to probe the chemical environments of unpaired electrons in condensed phase.[57] More specifically, the measured *g*-matrix quantifies the response of an electron spin to an external magnetic field, while the *A*-tensor reflects the nucleus-electron hyperfine interaction. Since an isolated electron has an isotropic gyromagnetic ratio of $g_e = 2.0023$, any local electric current induced by an applied

magnetic field will introduce an anisotropy into the *g*-matrix whose principal components may also be reduced due to magnetic shielding. Within the framework of generalized variational density functional perturbation theory,[58] the *g*-matrix can be calculated by the continuous set of gauge transformation (CSGT) approach[59] that warrants topologically well-behaved induced current density profile. Our EPR simulation is performed on RT5, which is selected for its rather complete charge and hence spin delocalization as underscored by its effective polaron radius of 0.77Å. Moreover, the all-electron polarized-valence-double-ζ (AE-PVDZ) basis set[45] is adopted to account for the significant contributions of core electrons to the induced electromagnetic fields.[60] As a further evidence of the anisotropy of polaron charge delocalization, our calculated $\Delta g = g - g_e$ has its greatest component along the major principal axis of [001] with $\Delta g_y = -0.0488$ (Table 2). By contrast, the components along the two minor principal axes of [110] and [1 $\bar{1}$ 0] are much smaller, assuming values of $\Delta g_x = -0.0195$ and $\Delta g_z = -0.0202$, respectively. Compared to the EPR spectrum,[48] our calculated principal values of Δg are all less than 15% off their experimental counterparts of $\Delta g_x = -0.0216$, $\Delta g_y = -0.0460$ and $\Delta g_z = -0.0237$. As anticipated, all principal axes coincide with high-symmetry directions in the supercell that can be ascribed to the relative displacements between neighboring titanium atoms. According to the crystal field theory,[61] metal-ligand coordination provokes the energy-level splitting of *d* orbitals in transition-metal atoms. In crystals with octahedral symmetry, such as rutile, the five *d* orbitals in the order of ascending energy are $|x^2 - y^2\rangle$, $|xz\rangle$, $|yz\rangle$, $|xy\rangle$ and $|z^2\rangle$. Since Ti^{3+} cation assumes an electronic configuration of $[\mathrm{Ar}]\mathrm{d}^1$, it is not surprising that the HOMO of the RT5 system

consists of a set of $|x^2-y^2\rangle$ orbitals, which are centered on the pivotal reduced complex and its nearest neighbors as depicted in Fig. 7. Under the first-order approximation[62] of the spin-orbit coupling, Δg is related to the spin-orbit constant, λ, and the energy gaps between the five *d* orbitals:

$$\Delta g_{ij} = -2\lambda \sum_{n \neq G} \frac{\langle G|\hat{L}_i|n\rangle\langle n|\hat{L}_j|G\rangle}{E_n - E_G} \qquad (6)$$

where $\hat{L}$ is the angular momentum operator, E_G and E_n are the energies of the ground and higher *d* orbitals, respectively. Given the principal axes of the *g*-matrix as listed in Table 2, the corresponding principal components can be expressed as

$$g_x = g_e - \frac{2\lambda}{\delta_2},\ g_y = g_e - \frac{2\lambda}{\delta_1},\ g_z = g_e - \frac{8\lambda}{\delta_3} \qquad (7)$$

where the energy gaps (δ_1,δ_2 and δ_3) are illustrated in Fig. 8. In light of the notable covalency of the Ti-O bonds, an orbital reduction factor, η, must be introduced to attenuate the spin-orbit coupling constant, λ, which is proportional to $r_{Ti^{3+}}^{-3}$ for a hydrogenetic Ti^{3+} cation.[63] Because the effective polaron radius in RT5 is 0.77Å, the reduced λ is given by $\left(\frac{r_0}{0.77\text{Å}}\right)^3 \lambda_0 \approx 0.012$ eV, where $\lambda_0 = 0.019$ eV is the spin-orbit coupling constant[64] for an isolated Ti^{3+} cation and r_0 is its radius of 0.66Å. Then, by solving Eq.7 using this value of λ, the *d*-orbital energy gaps are found to be $\delta_1 = 0.49$ eV, $\delta_2 = 1.19$ eV, and $\delta_3 = 4.93$ eV, all of which are in good agreement with the experimental values of $\delta_1 = 0.50$ eV, $\delta_2 = 0.97$ eV, and $\delta_3 = 4.24$ eV except for δ_3. The overestimation of δ_3 may arise from the orbital mixing between $|x^2-y^2\rangle$ and $|z^2\rangle$ that usually occurs in the orthorhombic crystal field of distorted rutile lattice[65] but is not

considered in the present study. As a final crosscheck with experiment, the *A*-tensor of ^{17}O atoms in RT5 is calculated by accounting for both the Fermi-contact interaction and dipole-dipole coupling. Because there are two groups of inequivalent ^{17}O atoms with respect to the pivotal Ti atom, two sets of calculated *A*-tensor are listed in Table 3. For a type 1 ^{17}O atom that bridges the pivotal reduced complex and its nearest [001] counterparts, the principal components of the calculated *A*-tensor are $A_x = 2.50\text{MHz}, A_y = 8.84\text{MHz}$ and $A_z = 6.01\text{MHz}$. Therefore, The isotropic hyperfine coupling constant defined as $A_{iso} = \frac{1}{3}\left(A_x + A_y + A_z\right)$ is calculated to be 5.78 MHz. By contrast, a type 2 ^{17}O atom, which is along the [110] direction, has a much smaller A_{iso} of 1.67 MHz due to the diminished electron spin density near its nucleus. The notable difference on the spin-orbit coupling strength between the two types of ^{17}O atoms has been revealed by a hyperfine sublevel correlation (HYSCORE) spectrum that affords $A_{iso}\left(\text{type 1 }^{17}\text{O}\right) = 8.0$ MHz and $A_{iso}\left(\text{type 2 }^{17}\text{O}\right) = 1.5$ MHz.[66] Note that our calculated A_{iso}s are somehow subject to the variance of on-site Hubbard potential, U, due to different levels of spin localization as suggested by previous theoretical[67] and experimental[68] studies. Specifically, when U changes from 2.5 eV to 3.5 eV, both A_{iso}s increase by more than 0.7 MHz whereas they decrease by a similar amount if U drops from 2.5 eV to 1.5 eV (Supporting Information S4). Moreover, as pointed out by a review article,[69] a reduced titanium cation may reside in a different chemical environment than the crystal lattice of rutile, making the comparison with various EPR experiments a deliberate practice.

4. Conclusions:

In the present study, the migration of a self-trapped electron in bulk rutile is investigated by using a valence-bond representation[38], which resorts to CDFT[39] for desired charge constraints before the evaluation of diabatic energies and electronic coupling strengths. It is found that the delocalization of polaron charge predominantly proceeds along the *c* crystal axis, effectively immobilizing the polaron on the *ab* crystal plane. Therefore, the electron polaron can be treated as a linear chain of titanium-centered anionic complexes, whose net charges drop considerably over their distances to the pivotal reduced complex. Due to the polaron's extensive charge delocalization, its extrapolated activation energy along the [001] lattice vector is as small as 0.026 eV, explaining the thermal instability of Ti^{3+} cation as observed in EPR experiments.[48] Moreover, the anisotropy of the shallow polaron is also revealed by our calculated *g*-matrix, whose principal component along [001] is much smaller than that along [110] or $[1\,\bar{1}\,0]$. As a measure of an unpaired electron's spatial extent, our calculated isotropic hyperfine constants of 5.78 MHz and 1.67 MHz for the two types of inequivalent ^{17}O atoms are in good agreement with the hyperfine sublevel correlation spectrum data,[66] further validating our simple yet reliable valence-bond model. Rutile, as the most abundant TiO_2 polymorph, is known to exhibit higher electron mobility and more pronounced directional heterogeneity in bulk phase than anatase and brookite. For the first time ever, the polaron delocalization in rutile is rigorously quantified by first-principle simulation to justify those unique traits, which are highly desired for a wide range of photovoltaic and photocatalytic applications.

Acknowledgements

The research was supported by a start-up grant and the Columbian College Facilitating Fund of the George Washington University. Computational resources utilized in this research were provided by the Argonne Leadership Computing Facility (ALCF) at Argonne National Laboratory under Department of Energy contract DE-AC02-06CH11357 and by the Extreme Science and Engineering Discovery Environment (XSEDE) at Texas Advanced Computing Center under National Science Foundation contract TG-CHE130008.

Figures:

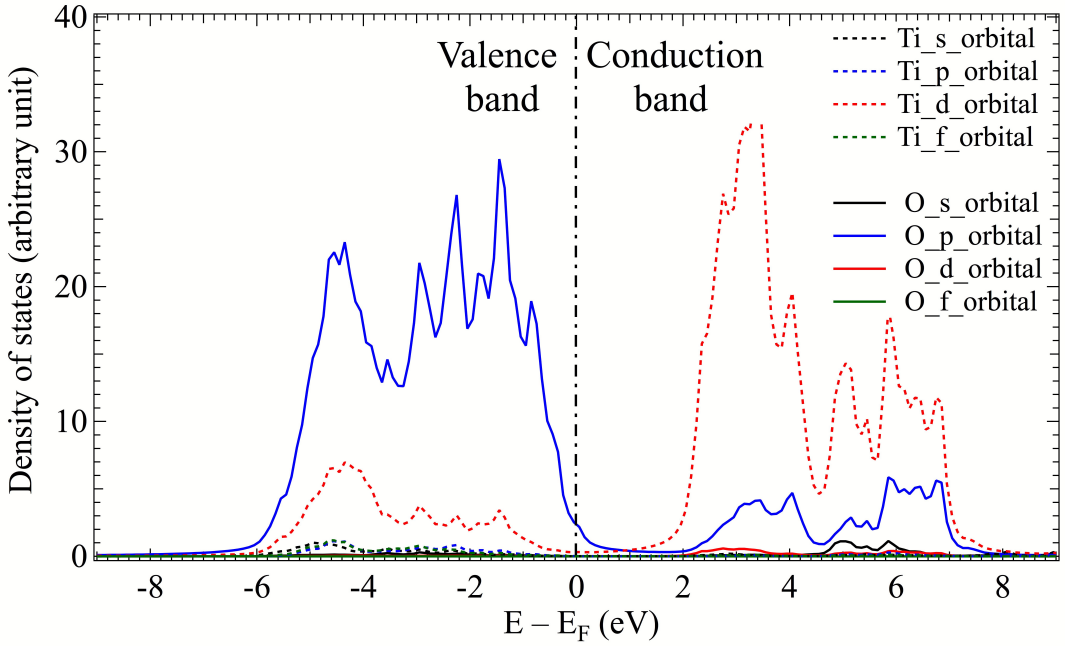

Figure 1. Calculated partial density of states for bulk rutile. E_F is the Fermi energy.

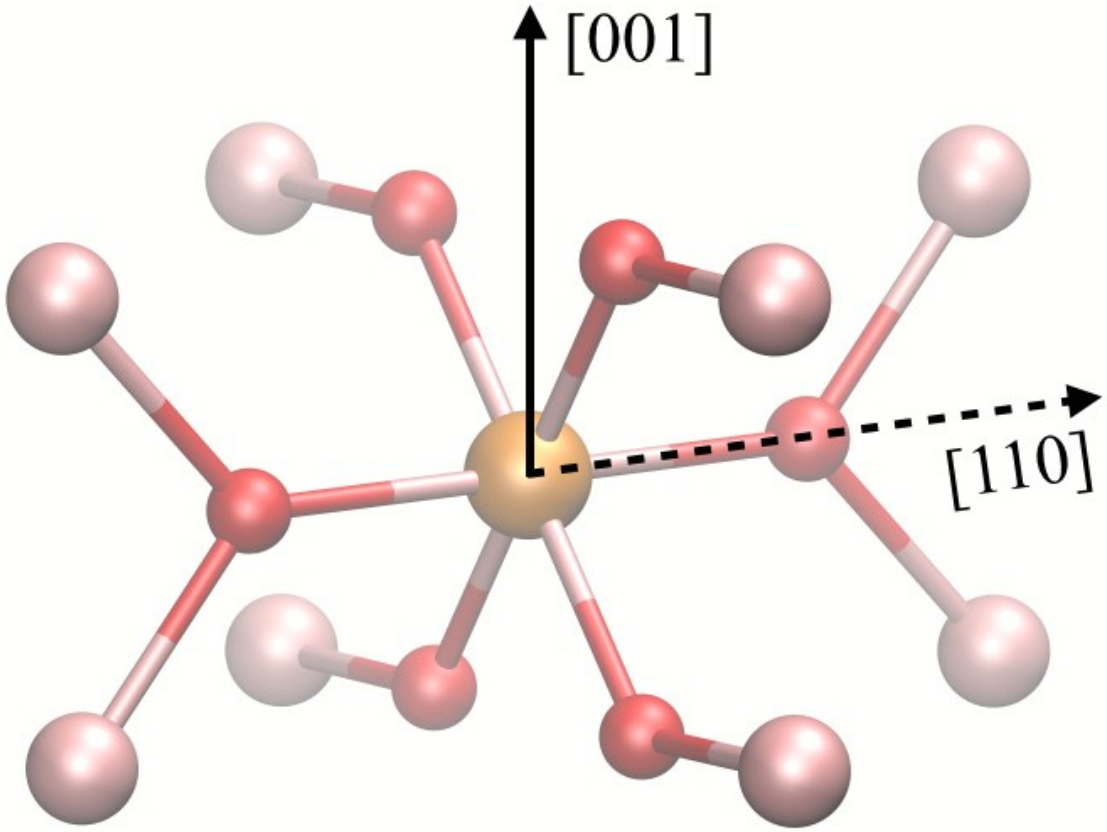

Figure 2. An electron (or anionic) single-site complex in bulk rutile. The pivotal titanium atom is colored orange, and its six coordinated oxygen atoms are colored red.

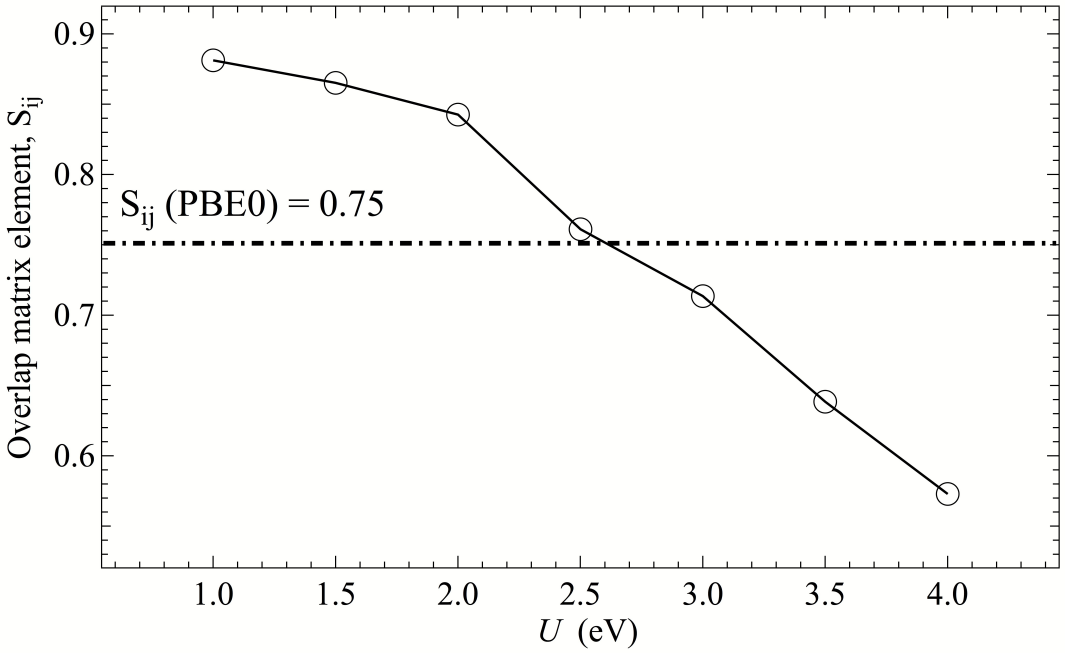

Figure 3. Benchmark results for the on-site Hubbard potential, U, with respect to the PBE0 hybrid functional for the overlap matrix element, S_{ij}, between two complexes along the [001] lattice vector in bulk rutile.

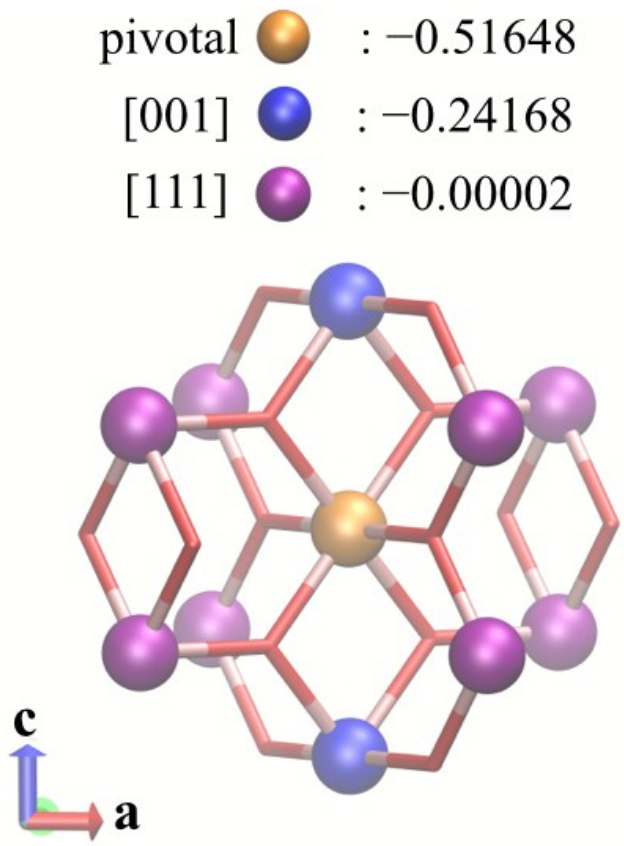

Figure 4. Polaron charge distribution across all single-site complexes that are bridged to the pivotal reduced complex (colored orange) through shared oxygen atoms. Each complex is represented by depicting its pivotal atom as a solid sphere. The lattice vectors of the single-site complexes with respect to the pivotal reduced complex are also listed. Note that a lattice vector of $[n_a n_b n_c]$ is chemically identical to that of $[n_b n_a n_c]$ because the crystal axes of a and b are equivalent in rutile.

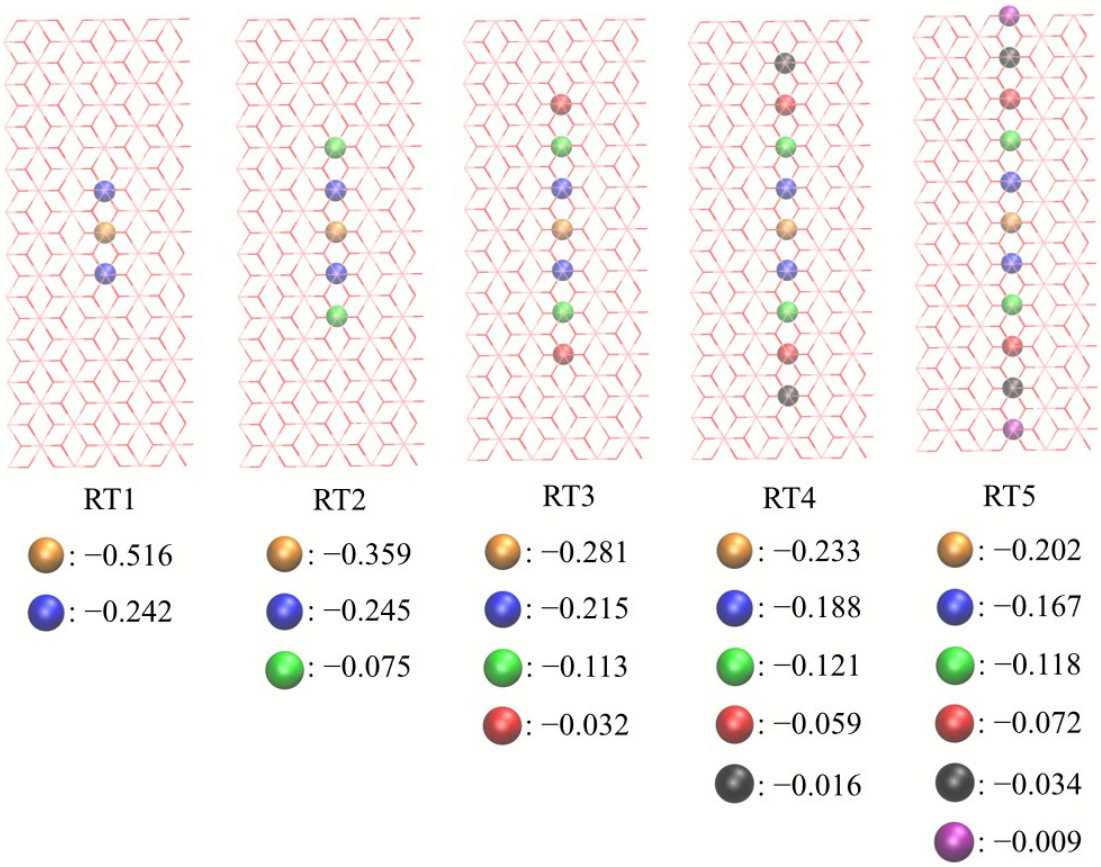

Figure 5. Delocalization of polaron charge with increasing number of participant complexes, each of which is represented by its pivotal atom as a solid sphere. The pivotal reduced complex is colored orange, while its 1st, 2nd, 3rd, 4th, and 5th nearest neighbors along the [001] lattice vector are colored blue, green, red, black and purple, respectively. See Supporting Information S2 for the Hamiltonian and overlap matrices used to determine the polaron charge distribution.

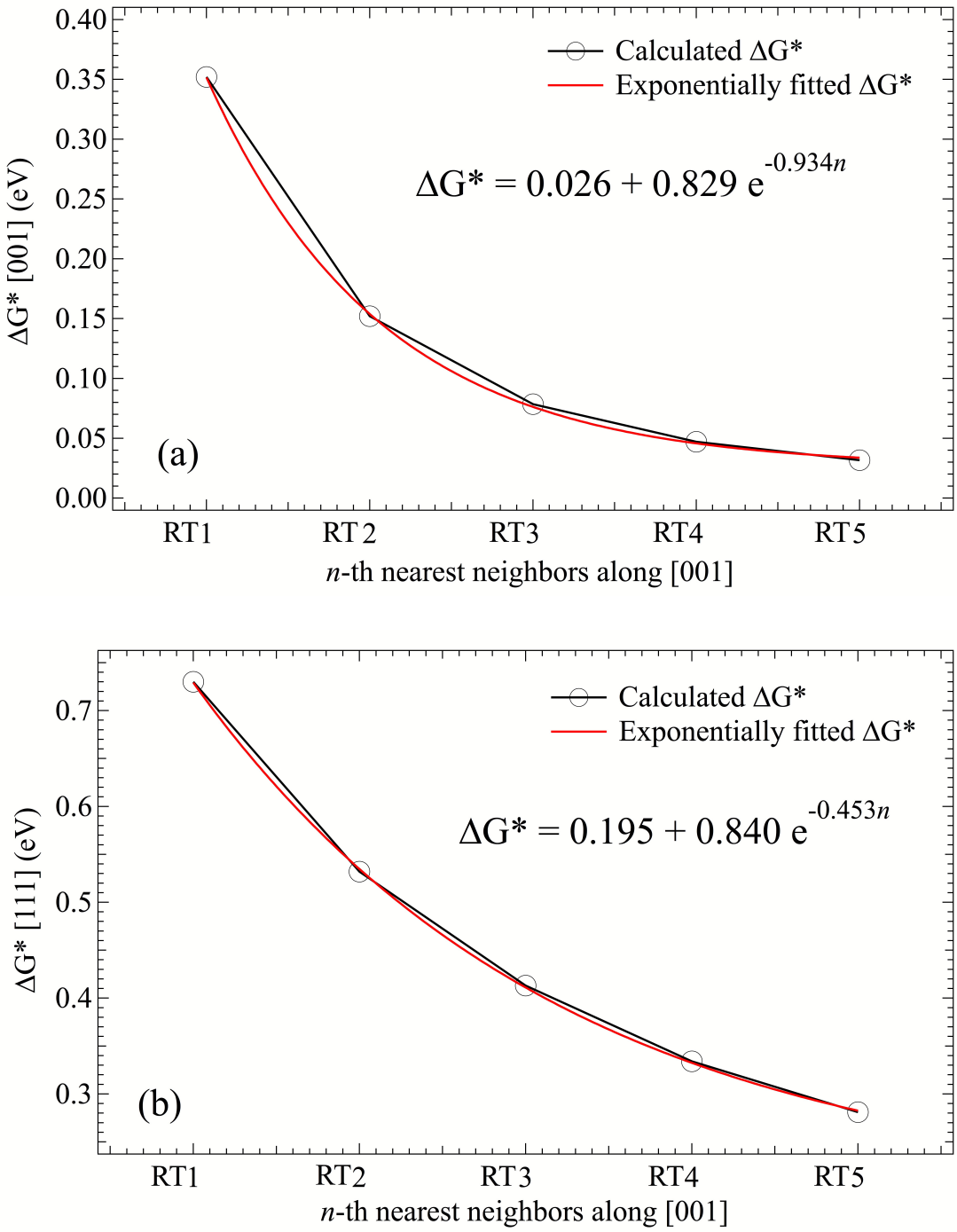

Figure 6. Calculated polaron activation energies, ΔG^*, along the [001] (panel a) and [111] (panel b) lattice vectors for the five RTn systems. The exponentially fitted activation energies are also shown in red.

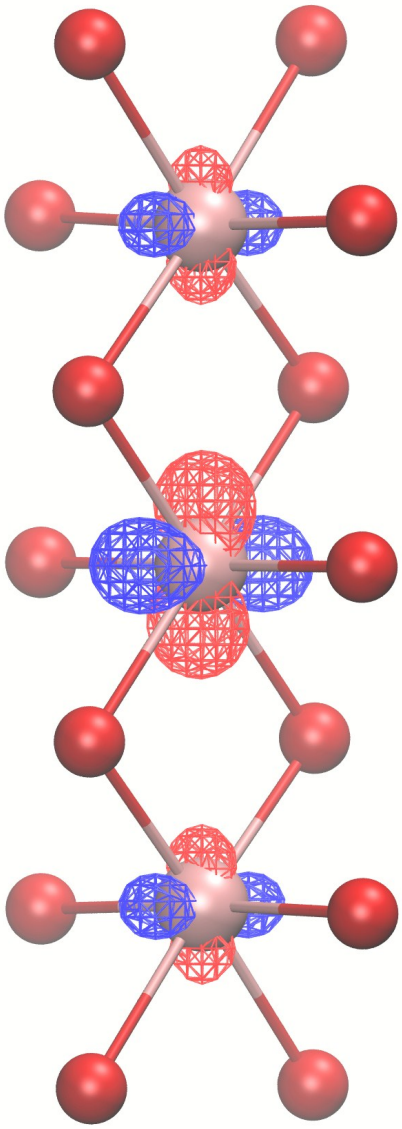

Figure 7. Isosurface of the highest occupied molecular orbital (HOMO) in the RT5 system.

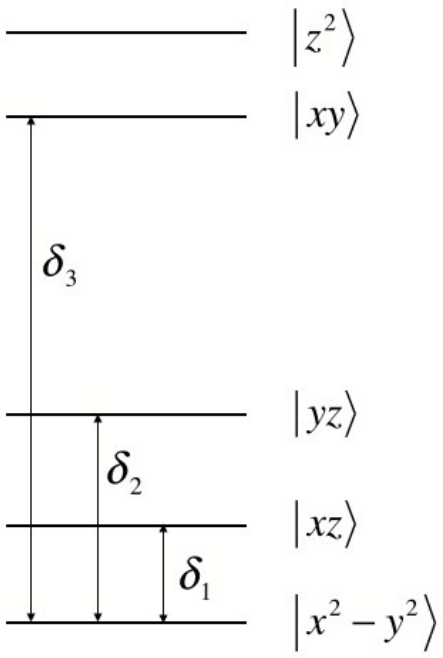

Figure 8. Relative ordering in energy of the five *d* orbitals on the Ti^{3+} cation.

Tables:

Lattice vector	**[001]**	**[111]**
ΔG^* (eV)	0.026	0.195
k_p (s^{-1})	5.56×10^{13}	8.05×10^{10}
n	2	8
R (Å)	2.96	3.57
μ ($cm^2/V\cdot s$)	3.77	0.0317

Table 1. Key migration properties for electron polaron at 300 K.

	g	$\Delta g = g - g_e$	principal axis
x	1.9828 (1.9807)	-0.0195 (-0.0216)	$[110]$
y	1.9535 (1.9563)	-0.0488 (-0.0460)	$[001]$
z	1.9821 (1.9786)	-0.0202 (-0.0237)	$[1\bar{1}0]$

Table 2. Principal elements of the calculated g-matrix for the RT5 system. The experimental values are also listed in the parentheses.

	Type 1 ^{17}O		Type 2 ^{17}O	
	A (MHz)	principal axis	A (MHz)	principal axis
x	2.50	$[110]$	2.30	$[110]$
y	8.84	$[001]$	1.59	$[001]$
z	6.01	$[1\bar{1}0]$	1.23	$[1\bar{1}0]$

Table 3. Principal components of the calculated A-tensor for type 1 and type 2 ^{17}O atoms in the RT5 system.

References:

1. Fujishima, A.; Honda, K., Electrochemical Photolysis of Water at a Semiconductor Electrode. *Nature* **1972**, *238*, 37-38.
2. Smith, S. J.; Stevens, R.; Liu, S.; Li, G.; Navrotsky, A.; Boerio-Goates, J.; Woodfield, B. F., Heat Capacities and Thermodynamic Functions of TiO_2 Anatase and Rutile: Analysis of Phase Stability. *Am. Mineral.* **2009**, *94*, 236-243.
3. Ranade, M. R.; Navrotsky, A.; Zhang, H. Z.; Banfield, J. F.; Elder, S. H.; Zaban, A.; Borse, P. H.; Kulkarni, S. K.; Doran, G. S.; Whitfield, H. J., Energetics of Nanocrystalline TiO_2. *Proc. Natl. Acad. Sci.* **2002**, *99*, 6476-6481.
4. Hanaor, D. H.; Sorrell, C., Review of the Anatase to Rutile Phase Transformation. *J. Mater. Sci.* **2011**, *46*, 855-874.
5. Howard, C. J.; Sabine, T. M.; Dickson, F., Structural and Thermal Parameters for Rutile and Anatase. *Acta Crystallogr. Sect. B.* **1991**, *47*, 462-468.
6. Rudnick, R. L.; Barth, M.; Horn, I.; McDonough, W. F., Rutile-Bearing Refractory Eclogites: Missing Link between Continents and Depleted Mantle. *Science* **2000**, *287*, 278-281.
7. Kapp, P.; Manning, C. E.; Tropper, P., Phase-Equilibrium Constraints on Titanite and Rutile Activities in Mafic Epidote Amphibolites and Geobarometry Using Titanite–Rutile Equilibria. *J. Metamorph. Geol.* **2009**, *27*, 509-521.
8. Miller, R., The Heavy Minerals of Florida Beach and Dune Sands. *Am. Mineral.* **1945**, *30*, 65-75.
9. Rams, J.; Tejeda, A.; Cabrera, J. M., Refractive Indices of Rutile as a Function of Temperature and Wavelength. *J. Appl. Phys.* **1997**, *82*, 994-997.
10. Tang, S.; Wang, J.; Zhu, Q.; Chen, Y.; Li, X., Preparation of Rutile TiO_2 Coating by Thermal Chemical Vapor Deposition for Anticoking Applications. *ACS Appl. Mater. Inter.* **2014**, *6*, 17157-17165.
11. Tiwald, T. E.; Schubert, M. In *Measurement of Rutile TiO_2 Dielectric Tensor from 0.148 to 33 mm Using Generalized Ellipsometry*, Proc. SPIE, San Diego, CA, The International Society for Optical Engineering: San Diego, CA, 2000; pp 19-29.
12. Hosaka, N.; Sekiya, T.; Satoko, C.; Kurita, S., Optical Properties of Single-Crystal Anatase TiO_2. *J. Phys. Soc. Jpn.* **1997**, *66*, 877-880.
13. Landmann, M.; Rauls, E.; Schmidt, W. G., The Electronic Structure and Optical Response of Rutile, Anatase and Brookite TiO_2. *J. Phys. Condens. Matter* **2012**, *24*, 195503-195508.
14. Al-Kattan, A.; Wichser, A.; Vonbank, R.; Brunner, S.; Ulrich, A.; Zuin, S.; Nowack, B., Release of TiO_2 from Paints Containing Pigment-TiO_2 or Nano-TiO_2 by Weathering. *Environ. Sci. Process. Impacts* **2013**, *15*, 2186-2193.
15. Popov, A. P.; Zvyagin, A. V.; Lademann, J.; Roberts, M. S.; Sanchez, W.; Priezzhev, A. V.; Myllylä, R., Designing Inorganic Light-Protective Skin Nanotechnology Products. *J. Biomed. Nanotechnol.* **2010**, *6*, 432-451.
16. Monteiro-Riviere, N. A.; Wiench, K.; Landsiedel, R.; Schulte, S.; Inman, A. O.; Riviere, J. E., Safety Evaluation of Sunscreen Formulations Containing Titanium Dioxide and Zinc Oxide Nanoparticles in UVB Sunburned Skin: An *in Vitro* and *in Vivo* Study. *Toxicol. Sci.* **2011**, *123*, 264-280.

17. Bogomolov, V. N.; Kudinov, E. K.; Firsov, Y. A., Polaron Nature of the Current Carriers in Rutile (TiO_2). *Sov. Phys. Solid State* **1968**, *9*, 2502-2513.
18. Cronemeyer, D. C., Electrical and Optical Properties of Rutile Single Crystals. *Phys. Rev.* **1952**, *87*, 876-886.
19. Ahmed, A. Y.; Kandiel, T. A.; Oekermann, T.; Bahnemann, D., Photocatalytic Activities of Different Well-Defined Single Crystal TiO_2 Surfaces: Anatase Versus Rutile. *J. Phys. Chem. Lett.* **2011**, *2*, 2461-2465.
20. Reinhardt, P.; Hess, B. A., Electronic and Geometrical Structure of Rutile Surfaces. *Phys. Rev. B* **1994**, *50*, 12015-12024.
21. Ahmed, A. Y.; Oekermann, T.; Lindner, P.; Bahnemann, D., Comparison of the Photoelectrochemical Oxidation of Methanol on Rutile TiO_2 (001) and (100) Single Crystal Faces Studied by Intensity Modulated Photocurrent Spectroscopy. *Phys. Chem. Chem. Phys.* **2012**, *14*, 2774-2783.
22. Perron, H.; Domain, C.; Roques, J.; Drot, R.; Simoni, E.; Catalette, H., Optimisation of Accurate Rutile TiO_2 (110), (100), (101) and (001) Surface Models from Periodic Dft Calculations. *Theor. Chem. Acc.* **2007**, *117*, 565-574.
23. Wallace, S. K.; McKenna, K. P., Grain Boundary Controlled Electron Mobility in Polycrystalline Titanium Dioxide. *Adv. Mater. Inter.* **2014**, *1*, 1400078-1400082.
24. Deskins, N. A.; Dupuis, M., Electron Transport Via Polaron Hopping in Bulk TiO_2: A Density Functional Theory Characterization. *Phys. Rev. B* **2007**, *75*, 195212-195221.
25. Setvin, M.; Franchini, C.; Hao, X.; Schmid, M.; Janotti, A.; Kaltak, M.; Van de Walle, C. G.; Kresse, G.; Diebold, U., Direct View at Excess Electrons in TiO_2 Rutile and Anatase. *Phys. Rev. Lett.* **2014**, *113*, 086402-086406.
26. Spreafico, C.; VandeVondele, J., The Nature of Excess Electrons in Anatase and Rutile from Hybrid DFT and RPA. *Phys. Chem. Chem. Phys.* **2014**, *16*, 26144-26152.
27. Emin, D.; Holstein, T., Studies of Small-Polaron Motion IV. Adiabatic Theory of the Hall Effect. *Ann. Phys.* **1969**, *53*, 439-520.
28. Austin, I. G.; Mott, N. F., Polarons in Crystalline and Non-Crystalline Materials. *Adv. Phys.* **2001**, *50*, 757-812.
29. Perdew, J. P.; Zunger, A., Self-Interaction Correction to Density-Functional Approximations for Many-Electron Systems. *Phys. Rev. B* **1981**, *23*, 5048-5079.
30. Heßelmann, A.; Görling, A., Random-Phase Approximation Correlation Methods for Molecules and Solids. *Mol. Phys.* **2011**, *109*, 2473-2500.
31. Ren, X.; Rinke, P.; Joas, C.; Scheffler, M., Random-Phase Approximation and Its Applications in Computational Chemistry and Materials Science. *J. Mater. Sci.* **2012**, *47*, 7447-7471.
32. Deskins, N. A.; Dupuis, M., Intrinsic Hole Migration Rates in TiO_2 from Density Functional Theory. *J. Phys. Chem. C* **2008**, *113*, 346-358.
33. Olsen, J., The Casscf Method: A Perspective and Commentary. *Int. J. Quantum Chem.* **2011**, *111*, 3267-3272.
34. Iordanova, N.; Dupuis, M.; Rosso, K. M., Theoretical Characterization of Charge Transport in Chromia (α-Cr_2O_3). *J. Chem. Phys.* **2005**, *123*, 074710-074720.
35. Schlosser, W., The Magnetovolume Effect in the Divalent Ions Mn^{2+} and Fe^{2+} and in Nis. *J. Phys. C. Solid State Phys.* **1976**, *9*, L19-L21.

36. VandeVondele, J.; Krack, M.; Mohamed, F.; Parrinello, M.; Chassaing, T.; Hutter, J., Quickstep: Fast and Accurate Density Functional Calculations Using a Mixed Gaussian and Plane Waves Approach. *Comput. Phys. Commun.* **2005**, *167*, 103-128.
37. Bezugly, V.; Birkenheuer, U., Multireference Configuration Interaction Treatment of Excited-State Electron Correlation in Periodic Systems: The Band Structure of Trans-Polyacetylene. *Chem. Phys. Lett.* **2004**, *399*, 57-61.
38. Yan, L.; Chen, H., Migration of Holstein Polarons in Anatase TiO_2. *J. Chem. Theory Comput.* **2014**, *10*, 4995-5001.
39. Wu, Q.; Van Voorhis, T., Extracting Electron Transfer Coupling Elements from Constrained Density Functional Theory. *J. Chem. Phys.* **2006**, *125*, 164105-164113.
40. Blöchl, P. E., Electrostatic Decoupling of Periodic Images of Plane-Wave Expanded Densities and Derived Atomic Point Charges. *J. Chem. Phys.* **1995**, *103*, 7422-7428.
41. Born, M.; Oppenheimer, R., Zur Quantentheorie Der Molekeln. *Annalen der Physik* **1927**, *389*, 457-484.
42. Farazdel, A.; Dupuis, M.; Clementi, E.; Aviram, A., Electric-Field Induced Intramolecular Electron Transfer in Spiro .Pi.-Electron Systems and Their Suitability as Molecular Electronic Devices. A Theoretical Study. *J. Am. Chem. Soc.* **1990**, *112*, 4206-4214.
43. Goedecker, S.; Teter, M.; Hutter, J., Separable Dual-Space Gaussian Pseudopotentials. *Phys. Rev. B* **1996**, *54*, 1703-1710.
44. Perdew, J. P.; Burke, K.; Ernzerhof, M., Generalized Gradient Approximation Made Simple. *Phys. Rev. Lett.* **1996**, *77*, 3865-3868.
45. Woon, D. E.; Dunning, T. H., Gaussian Basis Sets for Use in Correlated Molecular Calculations. Iv. Calculation of Static Electrical Response Properties. *J. Chem. Phys.* **1994**, *100*, 2975-2988.
46. Perdew, J. P.; Ernzerhof, M.; Burke, K., Rationale for Mixing Exact Exchange with Density Functional Approximations. *J. Chem. Phys.* **1996**, *105*, 9982-9985.
47. Stausholm-Møller, J.; Kristoffersen, H. H.; Hinnemann, B.; Madsen, G. K. H.; Hammer, B., DFT+U Study of Defects in Bulk Rutile TiO_2. *J. Chem. Phys.* **2010**, *133*, 144708-144715.
48. Yang, S.; Brant, A. T.; Giles, N. C.; Halliburton, L. E., Intrinsic Small Polarons in Rutile TiO_2. *Phys. Rev. B* **2013**, *87*, 125201-125206.
49. Pauling, L., *The Nature of the Chemical Bond and the Structure of Molecules and Crystals: An Introduction to Modern Structural Chemistry*; Cornell University Press: Ithaca, New York, 1960.
50. Iacconi, P.; Lapraz, D.; Caruba, R., Traps and Emission Centres in Thermoluminescent ZrO_2. *Phys. Status Solidi (a)* **1978**, *50*, 275-283.
51. Holstein, T., Studies of Polaron Motion: Part I. The Molecular-Crystal Model. *Ann. Phys.* **1959**, *8*, 325-342.
52. Holstein, T., Studies of Polaron Motion: Part II. The "Small" Polaron. *Ann. Phys.* **1959**, *8*, 343-389.
53. Yang, S.; Brant, A. T.; Halliburton, L. E., Photoinduced Self-Trapped Hole Center in Tio2 Crystals. *Phys. Rev. B* **2010**, *82*, 035209-035213.
54. Rodenhausen, H., Einstein's Relation between Diffusion Constant and Mobility for a Diffusion Model. *J. Stat. Phys.* **1989**, *55*, 1065-1088.

55. Porto, S. P. S.; Fleury, P. A.; Damen, T. C., Raman Spectra of TiO_2, MgF_2, ZnF_2, FeF_2, and MnF_2. *Phys. Rev.* **1967**, *154*, 522-526.
56. Hendry, E.; Koeberg, M.; O'Regan, B.; Bonn, M., Local Field Effects on Electron Transport in Nanostructured TiO_2 Revealed by Terahertz Spectroscopy. *Nano Lett.* **2006**, *6*, 755-759.
57. Freed, J. H., Electron Spin Resonance. *Annu. Rev. Phys. Chem.* **1972**, *23*, 265-310.
58. Putrino, A.; Sebastiani, D.; Parrinello, M., Generalized Variational Density Functional Perturbation Theory. *J. Chem. Phys.* **2000**, *113*, 7102-7109.
59. Keith, T. A.; Bader, R. F. W., Calculation of Magnetic Response Properties Using a Continuous Set of Gauge Transformations. *Chem. Phys. Lett.* **1993**, *210*, 223-231.
60. Weber, V.; Iannuzzi, M.; Giani, S.; Hutter, J.; Declerck, R.; Waroquier, M., Magnetic Linear Response Properties Calculations with the Gaussian and Augmented-Plane-Wave Method. *J. Chem. Phys.* **2009**, *131*, 014106-014116.
61. Van Vleck, J. H., Theory of the Variations in Paramagnetic Anisotropy among Different Salts of the Iron Group. *Phys. Rev.* **1932**, *41*, 208-215.
62. Wertz, J. E.; Bolton, J. R., *Electron Spin Resonance: Elementary Tehory and Practical Applications.*; McGraw-Hill: New York, 1972.
63. Blume, M.; Watson, R. E., Theory of Spin-Orbit Coupling in Atoms. I. Derivation of the Spin-Orbit Coupling Constant. *Proc. R. Soc. London, Ser. A.* **1962**, *270*, 127-143.
64. Kaufmann, U.; Rauber, A.; Schneider, J., EPR of Ti^{3+} in $CuAlS_2$. *J. Phys. C. Solid State Phys.* **1975**, *8*, L381-L383.
65. Gallay, R.; van der Klink, J. J.; Moser, J., EPR Study of Vanadium^{4+} in the Anatase and Rutile Phases of TiO_2. *Phys. Rev. B* **1986**, *34*, 3060-3068.
66. Livraghi, S.; Maurelli, S.; Paganini, M. C.; Chiesa, M.; Giamello, E., Probing the Local Environment of Ti^{3+} Ions in TiO_2 (Rutile) by ^{17}O HYSCORE. *Angew. Chem. Int. Ed.* **2011**, *50*, 8038-8040.
67. Finazzi, E.; Di Valentin, C.; Pacchioni, G.; Selloni, A., Excess Electron States in Reduced Bulk Anatase TiO_2: Comparison of Standard GGA, GGA+U, and Hybrid DFT Calculations. *J. Chem. Phys.* **2008**, *129*, 154113-154121.
68. Maurelli, S.; Livraghi, S.; Chiesa, M.; Giamello, E.; Van Doorslaer, S.; Di Valentin, C.; Pacchioni, G., Hydration Structure of the Ti(III) Cation as Revealed by Pulse EPR and DFT Studies: New Insights into a Textbook Case. *Inorg. Chem.* **2011**, *50*, 2385-2394.
69. Di Valentin, C.; Pacchioni, G.; Selloni, A., Reduced and N-Type Doped TiO_2: Nature of Ti^{3+} Species. *J. Phys. Chem. C* **2009**, *113*, 20543-20552.

TOC:

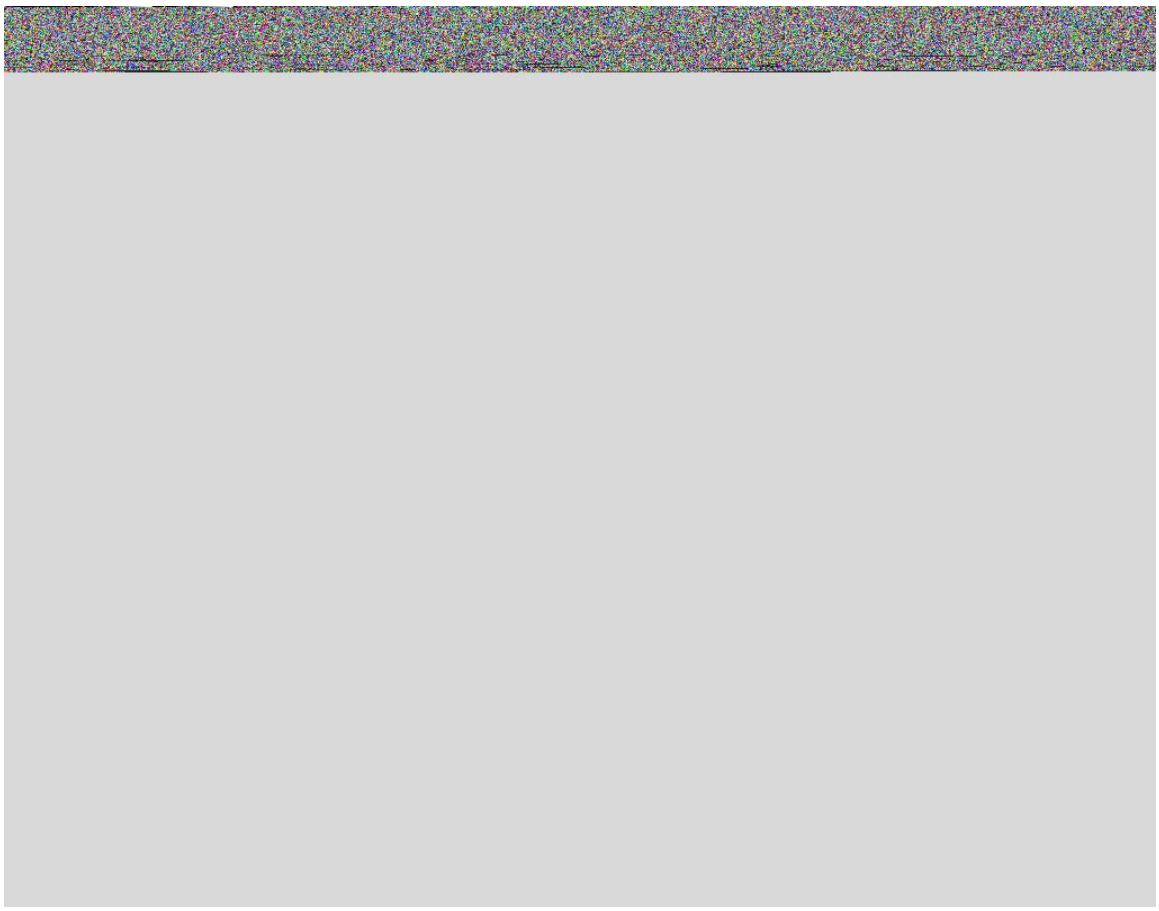

Anionic polaron migration in rutile TiO_2 is modeled by the valence bond representation in conjunction with the constrained density functional theory.